Novel version of bi input-extended Kalman filter for speed-sensorless control of induction motors with estimations of rotor and stator resistances, load torque, and inertia

Emrah ZERDALİ, Murat BARUT*
Department of Electrical and Electronics Engineering, Niğde University, Niğde, Turkey

Abstract: This study aims to develop a novel version of bi input-extended Kalman filter (BI-EKF)-based estimation technique in order to increase the number of state and parameter estimations required for speed-sensorless direct vector control (DVC) systems, which perform velocity and position controls of induction motors (IMs). For this purpose, all states required for the speed-sensorless DVC systems, besides the stator resistance R_s, the rotor resistance R_r, the load torque t_L including the viscous friction term, and the reciprocal of total inertia $1/j_T$, are simultaneously estimated by the novel BI-EKF algorithm using the measured phase currents and voltages. The effectiveness of the proposed speed-sensorless DVC systems is tested by simulations under the challenging variations of R_s, R_r, t_L, j_T, and velocity/position reference. Later, the state and parameter estimations of the novel BI-EKF algorithm are confirmed with real-time experiments in a wide speed range. Finally, in both transient and steady states, a satisfactory estimation and control performance that make this study unique are achieved.

Key words: Induction motor, extended Kalman filter, sensorless control, rotor-stator resistance estimation, load torque estimation, inertia estimation

1. Introduction

The robustness of state estimations of induction motors (IMs) improves the performance of the speed-sensorless control of IMs. For a speed/position control application of IMs with speed/position-sensorless, estimations of the rotor angular velocity/rotor position and the flux are required; however, these estimations are negatively affected by the variations in IM parameters, particularly the temperature and frequency-based variations of stator (R_s) and rotor (R_r) resistances, as well as the unknown load torque (t_L). In the literature, two groups of studies have been conducted utilizing the two-phase IM model for velocity estimation. The first group [1] assumes a slower variation of velocity with respect to the electrical states, and then defines velocity as a constant state that does not need the knowledge of t_L, inertia (j_T), and total viscous friction coefficient (β_T), yet gives rise to performance deterioration, especially in the transient state of the speed-sensorless control system. Unlike the first group, in the second group of studies, as in [2], velocity is estimated as a state with the utilization of the equation of motion in order to improve both the transient and the steady state performances of the speed-sensorless control system. However, the equation of motion requires accurate knowledge of t_L, j_T, and β_T.

---

*Correspondence: muratbarut27@yahoo.com

Recently, speed-sensorless studies as in [3–8] have been proposed. [3,4] are sensitive to R_r and R_s variations, whereas [5,6] and [7,8] are easily affected by the R_s and R_r variations, respectively. In studies such as [9–13], both R_s and R_r estimations were performed for a speed-sensorless control of IMs. However, the results presented in [9–11], which take place in the first group of studies, are sensitive to load torque variations. [12,13] are only applicable whenever the speed-sensorless control system is in steady-state, as declared by the authors.

The literature also includes extended Kalman filter (EKF)-based solutions, investigated by the switching/braided EKF- [14–17] and the BI-EKF-based [18] studies. These studies conduct simultaneous estimations of R_r, R_s, and t_L, including the viscous friction term ($\beta_T \times \omega_m$) together with stator currents, ω_m, and flux estimations, by using the measured stator phase currents and voltages. In [14–18], the total number of estimated states and parameters is 8. Later, [19] introduces a novel version of the BI-EKF algorithm-estimating stator currents, rotor fluxes, R_r, R_s, ω_m, and t_L, including the viscous friction term ($\beta_T \times \omega_m$) and $1/j_T$, in order to increase the number of the estimated states and varying parameters, which is 9 in [19]. However, [19] tests the effectiveness of the proposed estimation algorithm under the speed control of IM instead of using the position control systems where the speed of IM is zero or ultra-low, and the inertia information or estimation is vital. Moreover, [20] specifically aims to be capable of working in the field-weakening region; this type of operation requires the speed control of IM beyond its base/nominal speed, and causes variations in L_m. Therefore, the study in [20] simultaneously estimates L_m together with the estimations of stator currents, rotor fluxes, R_r, R_s, ω_m, and t_L, including the viscous friction term ($\beta_T \times \omega_m$) with the utilization of the novel version of the BI-EKF technique introduced in [19].

The major contribution of this study is to present a novel version of the BI-EKF-based estimation techniques, providing an increased number of state-parameter estimations and comparing it with its previous version in [18] for speed-sensorless DVC systems, which carry out both velocity and position controls of IMs. The novel BI-EKF-based estimator introduced in this study executes the simultaneous estimations of R_r, R_s, t_L including the viscous friction term, $1/j_T$ besides stator currents, ω_m, and rotor flux, by assuming that stator phase voltages and currents are available. From this point of view, it is the first known study in the literature and an extended version of the study in [19] that does not include the speed-sensorless position control system of the IM and its results. In addition, the comparisons made show the superiority of the proposed BI-EKF algorithm in this study over the previous study [17]. The simulations are conducted under the step-like variations of R_s, R_r, t_L, j_T, and velocity/position reference in order to show the validity of the proposed BI-EKF-based speed-sensorless control systems. The obtained results confirm a satisfactory estimation and control performance in both transient and steady states.

This paper is organized into six sections. Following the introduction in Section 1, Section 2 proceeds with the derivation of the extended IM models developed for $R_s\&t_L$ or $R_r\&\gamma_T$ estimations, together with all the states required for the speed-sensorless DVC systems. Next, Section 3 explains the novel BI-EKF technique. Section 4 presents two different speed-sensorless DVC systems established for velocity or position control of IM, respectively. In Section 5, the simulation results are provided to demonstrate the effectiveness of the novel BI-EKF algorithm and, hence, of speed-sensorless DVC systems. In Section 6, real-time experimental results validate the state and parameter estimations of the novel BI-EKF algorithm. Finally, the conclusions are given in Section 7.

2. Development of extended IM models

In this study, two extended rotor flux-based IM models are established for BI-EKF-based estimations in order to solve the simultaneous estimation problem of R_s, R_r, t_L, $\gamma_T \hat{=} 1/j_T$, and ω_m, as well as $i_{s\alpha}$, $i_{s\beta}$, $\varphi_{r\alpha}$, and $\varphi_{r\beta}$. For this aim, the extended models in discrete form, proposed in this study as Model 1 [14,15,17,18,20] and Model 2 for the R_r and γ_T estimations, can be given (as referred to the stator stationary frame) in the following general form:

$$
\begin{aligned}
\underline{x}_{ei}(k+1) &= \underline{f}_{ei}(\underline{x}_{ei}(k), \underline{u}_e(k)) + \underline{w}_{i1}(k) \\
&= \underline{A}_{ei}(\underline{x}_{ei}(k))\underline{x}_{ei}(k) + \underline{B}_e \underline{u}_e(k) + \underline{w}_{i1}(k)
\end{aligned}
\tag{1}
$$

$$
\begin{aligned}
\underline{Z}(k) &= \underline{h}_{ei}(\underline{x}_{ei}(k)) + \underline{w}_{i2}(k) \text{ (measurement equation)} \\
&= \underline{H}_e \underline{x}_{ei}(k) + \underline{w}_{i2}(k)
\end{aligned}
\tag{2}
$$

Here $i = 1$ or 2 represents each model, $\underline{x}_{ei}$ is the extended state vector for both models, $\underline{f}_{ei}$ is the nonlinear function of the states and inputs, $\underline{A}_{ei}$ is the system matrix, $\underline{u}_e$ is the control input vector, $\underline{B}_e$ is the input matrix, $\underline{w}_{i1}$ is the process noise, $\underline{h}_{ei}$ is the function of the outputs, $\underline{H}_e$ is the measurement matrix, and $\underline{w}_{i2}$ is the measurement noise. Subject to the general form in Eqs. (1) and (2), the matrices or vectors in the two extended IM models can be represented as follows:

- Model 1: The extended IM model [14,15,17,18,20] developed for R_s and t_L estimations (Model-$R_s \& t_L$).

$$
\underline{x}_{e1} = [\; i_{s\alpha}(k) \quad i_{s\beta}(k) \quad \varphi_{r\alpha}(k) \quad \varphi_{r\beta}(k) \quad \omega_m(k) \quad t_L(k) \quad R_s(k) \;]^T
$$

$$
\underline{A}_{e1} \hat{=}
\begin{bmatrix}
1 - \left(\frac{R_s(k)}{L_\sigma} - \frac{L_m^2 R_r}{L_\sigma L_r^2} \right) T & 0 & \frac{L_m R_r T}{L_\sigma L_r^2} & \frac{L_m p_p T \omega_m(k)}{L_\sigma L_r} & 0 & 0 & 0 \\
0 & 1 - \left(\frac{R_s(k)}{L_\sigma} - \frac{L_m^2 R_r}{L_\sigma L_r^2} \right) T & -\frac{L_m p_p T \omega_m(k)}{L_\sigma L_r} & \frac{L_m R_r T}{L_\sigma L_r^2} & 0 & 0 & 0 \\
\frac{L_m R_r T}{L_r} & 0 & 1 - \frac{R_r T}{L_r} & -p_p T \omega_m(k) & 0 & 0 & 0 \\
0 & \frac{L_m R_r T}{L_r} & p_p T \omega_m(k) & 1 - \frac{R_r T}{L_r} & 0 & 0 & 0 \\
-\frac{3}{2} \frac{L_m}{L_r} \frac{p_p}{J_T} T \varphi_{r\beta}(k) & \frac{3}{2} \frac{L_m}{L_r} \frac{p_p}{J_T} T \varphi_{r\alpha}(k) & 0 & 0 & 1 & -\frac{T}{J_T} & 0 \\
0 & 0 & 0 & 0 & 0 & 1 & 0 \\
0 & 0 & 0 & 0 & 0 & 0 & 1
\end{bmatrix}
$$

- Model 2: The extended IM model introduced for R_r and γ_T estimations (Model-$R_r \& \gamma_T$) in this study.

$$
\underline{x}_{e2} = [\; i_{s\alpha}(k) \quad i_{s\beta}(k) \quad \varphi_{r\alpha}(k) \quad \varphi_{r\beta}(k) \quad \omega_m(k) \quad \gamma_T(k) \quad R_r(k) \;]^T
$$

$$
\underline{A}_{e2} \hat{=}
\begin{bmatrix}
1 - \left(\frac{R_s}{L_\sigma} - \frac{L_m^2 R_r(k)}{L_\sigma L_r^2} \right) T & 0 & \frac{L_m R_r(k) T}{L_\sigma L_r^2} & \frac{L_m p_p T \omega_m(k)}{L_\sigma L_r} & 0 & 0 & 0 \\
0 & 1 - \left(\frac{R_s}{L_\sigma} - \frac{L_m^2 R_r(k)}{L_\sigma L_r^2} \right) T & -\frac{L_m p_p T \omega_m(k)}{L_\sigma L_r} & \frac{L_m R_r(k) T}{L_\sigma L_r^2} & 0 & 0 & 0 \\
\frac{L_m R_r(k) T}{L_r} & 0 & 1 - \frac{R_r(k) T}{L_r} & -p_p T \omega_m(k) & 0 & 0 & 0 \\
0 & \frac{L_m R_r(k) T}{L_r} & p_p T \omega_m(k) & 1 - \frac{R_r(k) T}{L_r} & 0 & 0 & 0 \\
-\frac{3}{2} \frac{L_m}{L_r} p_p \varphi_{r\beta}(k) \gamma_T(k) & \frac{3}{2} \frac{L_m}{L_r} p_p \varphi_{r\alpha}(k) \gamma_T(k) & 0 & 0 & 1 & -t_L T & 0 \\
0 & 0 & 0 & 0 & 0 & 1 & 0 \\
0 & 0 & 0 & 0 & 0 & 0 & 1
\end{bmatrix}
$$

- In both models, $\underline{B}_e$, $\underline{u}_e$, $\underline{H}_e$, and the coefficients are given by

$$\underline{B}_e = \left[\begin{array}{ccccccc} \frac{T}{L_\sigma} & 0 & 0 & 0 & 0 & 0 & 0 \\ 0 & \frac{T}{L_\sigma} & 0 & 0 & 0 & 0 & 0 \end{array} \right]^T, \underline{u}_e = \left[\begin{array}{cc} v_{s\alpha}(k) & v_{s\beta}(k) \end{array} \right]$$

$$\underline{H}_e = \left[\begin{array}{ccccccc} 1 & 0 & 0 & 0 & 0 & 0 & 0 \\ 0 & 1 & 0 & 0 & 0 & 0 & 0 \end{array} \right],$$

where j_T is the total inertia of the IM and load; γ_T is defined as $1/j_T$; ω_m is the rotor angular velocity; p_p is the number of pole pairs; $L_\sigma = \sigma L_s$ is the stator transient inductance; $\sigma = 1 - \frac{L_m^2}{L_s L_r}$ is the leakage or coupling factor; L_s and L_r are the stator and rotor inductances, respectively; $\varphi_{r\alpha}$ and $\varphi_{r\beta}$ are the stator stationary axis components of rotor fluxes; $v_{s\alpha}$ and $v_{s\beta}$ are the stator stationary axis components of stator voltages; $i_{s\alpha}$ and $i_{s\beta}$ are the stator stationary axis components of stator currents; and T is the sampling time.

In Model-$R_s \& t_L$ and Model-$R_r \& \gamma_T$,

- the main difference occurs due to the constant states $R_s \& t_L$ in $\underline{x}_{e1}$ and $R_r \& \gamma_T$ in $\underline{x}_{e2}$, respectively.

- $\underline{w}_{11}$ and $\underline{w}_{22}$ in Eq. (2) are equal, because they use the same measured state variables, $i_{s\alpha}$ and $i_{s\beta}$.

3. Theoretical foundations of the novel BI-EKF algorithm

The BI-EKF algorithm in this study simultaneously estimates R_s, R_r, t_L, γ_T, and ω_m as well as $\varphi_{r\alpha}$, $\varphi_{r\beta}$, $i_{s\alpha}$, and $i_{s\beta}$ by utilizing measured stator phase voltages and currents for a speed control application of IM. Thus, it has priority over previous BI-EKF-based studies, as in [18], which estimates the same parameters and states except for γ_T. In other words, the BI-EKF algorithm in this study estimates more parameters than other EKF-based or past studies.

To describe this type of BI-EKF technique, conventional EKF equations can be given as follows:

$$\underline{F}_{ei}(k) = \left. \frac{\partial \underline{f}_{ei}(\underline{x}_{ei}(k), \underline{u}_e(k))}{\partial \underline{x}_{ei}(k)} \right|_{\hat{\underline{x}}_{ei}(k), \underline{u}_e(k)} \tag{3a}$$

$$\underline{N}_i(k) = \underline{F}_{ei}(k)\underline{P}_i(k)\underline{F}_{ei}^T(k) + \underline{Q}_i \tag{3b}$$

$$\underline{P}_i(k+1) = \underline{N}_i(k) - \underline{N}_i(k)\underline{H}_e^T(\underline{D}_\xi + \underline{H}_e\underline{N}_i(k)\underline{H}_e^T)^{-1}\underline{H}_e\underline{N}_i(k) \tag{3c}$$

$$\hat{\underline{x}}_{ei}(k+1) = \hat{\underline{f}}_{ei}(\hat{\underline{x}}_{ei}(k), \underline{u}_e(k)) + \underline{P}_i(k+1)\underline{H}_e^T D_\xi^{-1}(\underline{Z}(k) - \underline{H}_e\hat{\underline{x}}_{ei}(k)) \tag{3d}$$

where $\underline{F}_{ei}$ is the function used in the linearization of the nonlinear models (1). $\underline{Q}_i$ is the covariance matrix of the system noise, namely the model error. $\underline{D}_\xi$ is the covariance matrix of the output noise, namely the measurement noise. $\underline{P}_i$ and $\underline{N}_i$ are the covariance matrix of the state estimation error and extrapolation error, respectively.

The BI-EKF algorithm (Figure 1) is finally established by considering the EKF equations (3a, 3b, 3c, and 3d) and exploiting the three remarks [18] as follows:
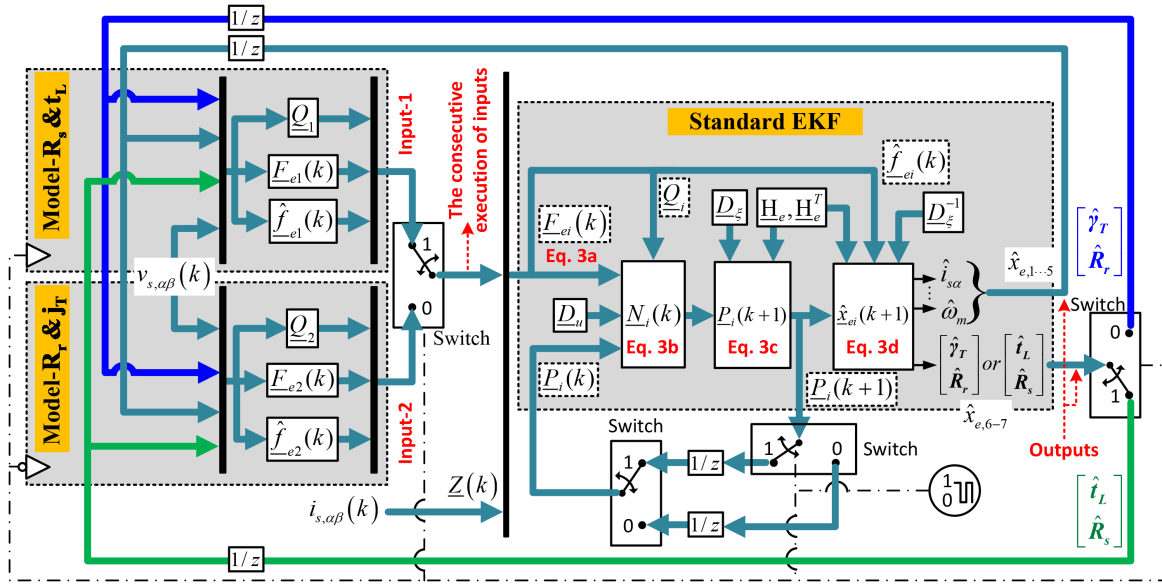
Figure 1. Flow chart of the novel BI-EKF algorithm.

Remark 1 *Eqs. 3b, 3c, and 3d constitute the main body of the EKF algorithm.*

Remark 2 *The inputs of Eqs. 3b, 3c, and 3d, which must be changed for Model 1 or Model 2, are $\underline{F}_{ei}$, $\underline{Q}_i$, and $\underline{\hat{f}}_{ei}$ because the elements of those matrices are calculated from each model.*

Remark 3 *The inputs of Eqs. 3b, 3c, and 3d, which must be the same for both models, are $\underline{D}_\zeta$ and $\underline{H}_e$, due to using the same measurements ($i_{s\alpha}$ and $i_{s\beta}$). Moreover, the dimensions of $\underline{N}_i$, $\underline{P}_i$ and $\underline{\hat{x}}_{ei}$ are identical for both models due to utilizing same-order models.*

As demonstrated in Figure 1, the BI-EKF algorithm is constructed on a single-standard EKF algorithm, consecutively using two different inputs calculated from Model-$R_s\&t_L$ and Model-$R_r\&\gamma_T$, respectively. Consequently, it is called bi input EKF (BI-EKF). The consecutive operation of the two inputs is performed at each sampling time (T). During each T, the simultaneous estimation of the same group of states ($i_{s\alpha}$, $i_{s\beta}$, $\varphi_{r\alpha}$, $\varphi_{r\beta}$, and ω_m) is executed additionally with $R_s\&t_L$ or $R_r\&\gamma_T$, respectively. At the end of each T, the estimated values of $R_s\&t_L$ or $R_r\&\gamma_T$ are utilized as a constant parameter in the other input, whereas the estimated values of $i_{s\alpha}$, $i_{s\beta}$, $\varphi_{r\alpha}$, $\varphi_{r\beta}$ and ω_m are updated to both inputs as initial values. Furthermore, $\underline{P}_i(k+1)$ is stored as $\underline{P}_i(k)$ for the usage of the next T.

Differently from the previous version of the BI-EKF algorithm, firstly reported in [18] and performing simultaneously the estimations of $i_{s\alpha}$, $i_{s\beta}$, $\varphi_{r\alpha}$, $\varphi_{r\beta}$, ω_m, t_L, R_s, and R_r, the novel BI-EKF technique introduced in this study provides a consecutive switching between two IM models with five states ($i_{s\alpha}$, $i_{s\beta}$, $\varphi_{r\alpha}$, $\varphi_{r\beta}$, and ω_m) plus two constant states/parameters ("t_L and R_s" or "R_r and γ_T"). For this reason, the novel version of the BI-EKF algorithm is able to estimate concurrently $i_{s\alpha}$, $i_{s\beta}$, $\varphi_{r\alpha}$, $\varphi_{r\beta}$, ω_m, t_L, R_s, R_r, and γ_T, which also renders this study unique.

4. Speed-sensorless DVC systems

In this study, the proposed BI-EKF algorithm is used in the combination of the two different speed-sensorless DVC systems designed for either velocity or position control of IMs, respectively, in order to verify its effectiveness. These speed-sensorless schemes are explained in the following sections.

4.1. Speed-sensorless DVC scheme for velocity control of IM

The block diagram of the novel BI-EKF-based speed-sensorless DVC system implemented in MATLAB Simulink for the velocity control of IM is shown in Figure 2. Here $\hat{\theta}_{rf}$ is the field angle defined between the α-axis of the stator stationary frame and the d-axis of the rotating frame; namely, the dq-frame is rotating at $d\hat{\theta}_{rf}/dt$. All controllers in the system are conventional PIs.

Figure 2. The novel BI-EKF-based speed-sensorless DVC of IMs.

4.2. Speed-sensorless DVC scheme for position control of IM

The proposed BI-EKF-based speed-sensorless DVC system developed for the position control of IM is illustrated in Figure 3. Here the sliding mode controllers (SMCs), SMC_1 and SMC_2, were previously developed in [17]. According to [17], the sliding manifolds σ_d and σ_q are defined for the field controller SMC_1 and the position controller SMC_2, respectively, as follows:

$$\sigma_d = |\vec{\varphi}_r|^{ref} - \varphi_{rd} \tag{4a}$$

$$\sigma_q = (\dot{\theta}_m^{ref} - \dot{\theta}_m) + c(\theta_m^{ref} - \theta_m) = \dot{e}_q + ce_q (c > 0) \tag{4b}$$

Figure 3. The novel BI-EKF-based sliding mode position control system.

To make SMC_1 and SMC_2 stable according to the Lyapunov theory, a positive definite Lyapunov function [17] is selected as

$$V = \frac{1}{2}\sigma_d^2 + \frac{1}{2}\sigma_q^2 \rightarrow \dot{V} = \sigma_d \dot{\sigma}_d + \sigma_q \dot{\sigma}_q \tag{5}$$

By combining the power rate reaching law in [21] and the average-equivalent control law in [22], the control laws for SMC_1 and SMC_2 are finally obtained in [17] as follows:

$$i_{sd}(k) = i_{sd}(k+1) + \frac{\sigma_d(k) - \sigma_d(k-1)}{\bar{k}_5 T} + \frac{k_d |\sigma_d(k)|^{1/n_d} sgn(\sigma_d(k))}{\bar{k}_5} \tag{6a}$$

$$i_{sq}(k) = i_{sq}(k-1) + \frac{\sigma_q(k) - \sigma_q(k-1)}{\bar{k}_7 T |\vec{\varphi}_r|^{ref}} + \frac{k_q |\sigma_q(k)|^{1/n_q} sgn(\sigma_q(k))}{\bar{k}_7 |\vec{\varphi}_r|^{ref}} \tag{6b}$$

(where $k_d > 0$, $k_q > 0$, $0 < n_d < 1$, $0 < n_q < 1$, $\bar{k}_5 = \frac{R_r}{L_r} L_m$, and $\bar{k}_7 = \frac{3}{2}\frac{p_p}{J_L}\frac{L_m}{L_r}$)

5. Simulation results

In our simulations, the proposed estimation algorithm and the speed-sensorless drives shown in Figures 2 and 3 were tested with the rated parameters in the Table. The values in the Table are the same as in [14,17,18], so that a reasonable comparison between the results in this study and those in [14,17,18] could be made.

Estimation and, hence, control performances are directly affected by the elements of the covariance matrices (Q_i, P_i, and D_ξ), which are time-varying and calculated from the statistical features of the corresponding noises in theory. From the application point of view, in this study it is assumed that:

- the values of Q_i, P_i, and D_ξ are constant, and Q_i, P_i, and D_ξ are in diagonal for reducing the computational load.

Table. The induction motor parameters used in the simulations.

$P\,[kW]$	3	$R_{sn}\,[\Omega]$	2.283
$f\,[Hz]$	50	$R_{rn}\,[\Omega]$	2.133
$j_{Tn}\,[kg.m^2]$	0.0183	$L_s\,[H]$	0.2311
$\beta_T\,[N.m/(rad/s)]$	0.001	$L_r\,[H]$	0.2311
p_p	2	$L_{mn}\,[H]$	0.22
$V\,[V]$	380	$n_{mn}\,[rpm]$	1430
$I\,[A]$	6.9	$t_{Ln}\,[N.m]$	20

- the first two values in the diagonal elements of Q_i are equal to each other, since they are associated with $i_{s\alpha}$ and $i_{s\beta}$ and have noise with the statistically same characteristic. The same idea is applied to the elements of Q_i associated with $\varphi_{r\alpha}$ and $\varphi_{r\beta}$.

Considering the assumptions made for the covariance matrices, mathematically small values are initially set into the covariance matrices; this means that the model and parameters of IM used in the EKF algorithm are good enough to represent the real IM, and the measurements are well done. In general, the desired transient and steady-state behaviors of the estimated states and parameters are obtained by regulating the elements of Q_i, whereas the rapid initial convergence of the EKF algorithm is tuned by the values of P_i. Thus, after very few attempts to achieve desired estimation accuracy, the covariance matrices in the novel BI-EKF algorithm in this study are easily determined with the trial-and-error method as follows:

$$Q_1 = diag\left\{\begin{array}{ccccccc} 10^{-9} & 10^{-9} & 10^{-9} & 10^{-9} & 10^{-7} & 10^{-4} & 10^{-5} \end{array}\right\}$$

$$Q_2 = diag\left\{\begin{array}{ccccccc} 10^{-9} & 10^{-9} & 10^{-9} & 10^{-9} & 10^{-7} & 10^{-2} & 10^{-5} \end{array}\right\}$$

$$P_i = diag\left\{\begin{array}{ccccccc} 9 & 9 & 9 & 9 & 9 & 9 & 9 \end{array}\right\}$$

$$D_\xi = diag\left\{\begin{array}{cc} 10^{-6} & 10^{-6} \end{array}\right\}$$

The design parameters used in the SMCs in Figure 3 are determined as follows:

$$k_d = 0.015, \ k_q = 0.010, \ n_d = n_q = 0.5, \ c = 17$$

In order to verify the BI-EKF algorithm, the simulations are conducted by using each speed-sensorless DVC system, and are evaluated in the next two sections.

5.1. Simulation results and observations for the speed-sensorless velocity control system

In order to verify the novel BI-EKF algorithm with the speed-sensorless velocity control system in Figure 2, the six different scenarios illustrated in Figure 4 are performed in simulations. These scenarios are orderly defined for certain time intervals as follows:
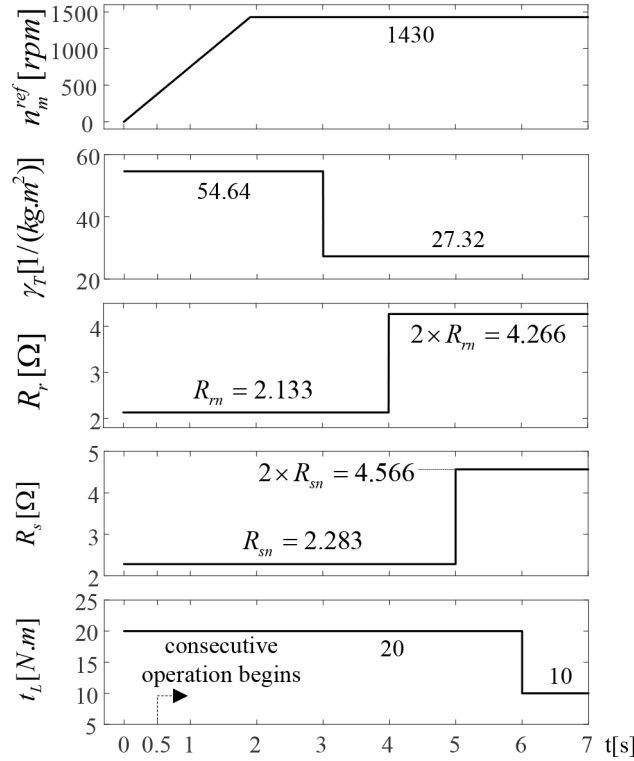
Figure 4. Variations of n_m^{ref}, the applied t_L, R_s, R_r, and γ_T for performance test.

- Firstly, the novel BI-EKF algorithm is given a start with incorrect $R_r = 0.5 \times R_{rn}$ and $\gamma_T = 0.5 \times \gamma_{Tn}$ under t_{Ln}, R_{sn}, and j_{Tn}, by using only Model-R_s&t_L $(0\,s \leq t \leq 0.5\,s)$.

- Secondly, the consecutive operation of the novel BI-EKF algorithm starts at $0.5\,s$, then the IM speeds up linearly to $1500\,rpm$ and is kept constant at $1500\,rpm$ $(0.5\,s \leq t \leq 3\,s)$.

- Thirdly, j_T is instantaneously increased to $2 \times j_{Tn}$ at $3\,s$; namely, γ_T is reduced to $0.5 \times \gamma_{Tn}$ while the IM is running at $1500\,rpm$ under t_{Ln}, R_{sn}, and R_{rn} $(3\,s \leq t \leq 4\,s)$.

- Fourthly, R_r is stepped up to $2 \times R_{rn}$ at $4\,s$ when the IM is operating at $1500\,rpm$ under t_{Ln}, R_{sn}, and $\gamma_T = 0.5 \times \gamma_{Tn}$ $(4\,s \leq t \leq 5\,s)$.

- Fifthly, R_s is abruptly increased to $2 \times R_{sn}$ at $5\,s$ $(5\,s \leq t \leq 6\,s)$.

- Sixthly, t_L is stepped down to $0.5 \times t_{Ln}$ at $6\,s$ while the IM is running at $1500\,rpm$ under $2 \times R_{sn}$, $2 \times R_{rn}$, and $0.5 \times \gamma_{Tn}$ $(6\,s \leq t \leq 7\,s)$.

These scenarios are developed by incurring simultaneous changes to j_T, R_r, R_s, and t_L of the IM shown in Figure 4, together with n_m^{ref}. The resulting estimation and control performances of the speed-sensorless *velocity* control system under the above scenarios are presented in Figures 5 and 6. In these figures, "^" represents estimated state or parameter, and error signal $e_{(.)}$ is defined as the difference between the actual and the estimated components.
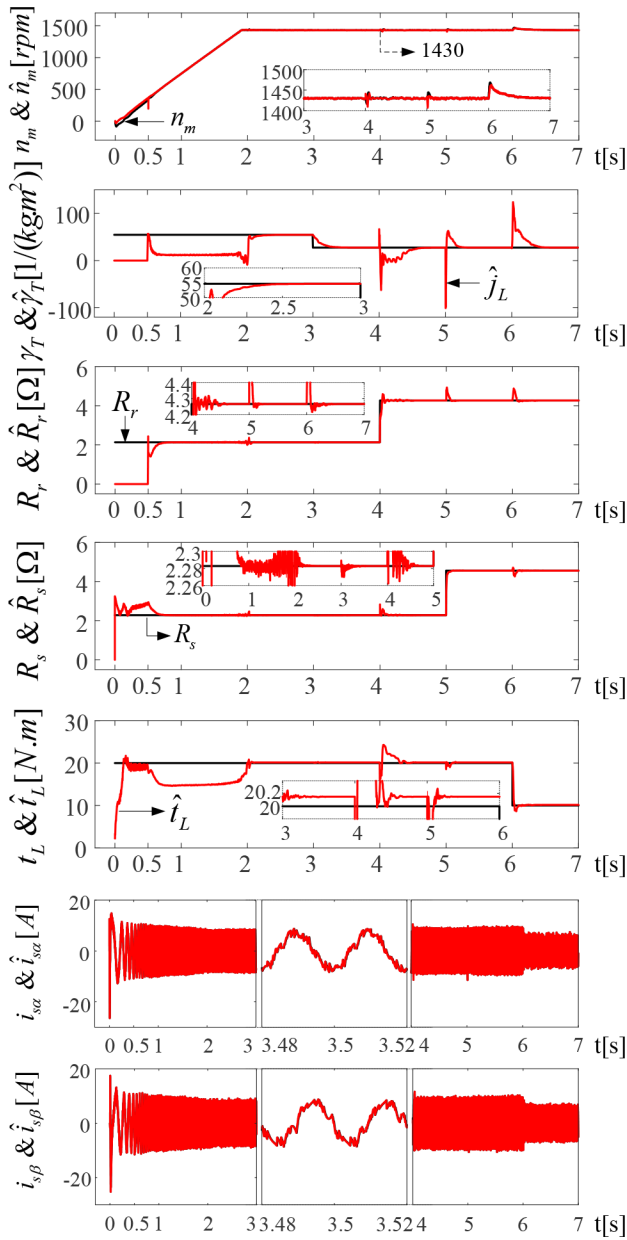
Figure 5. Simulation results of the novel BI-EKF-based estimator and the speed-sensorless velocity control system.
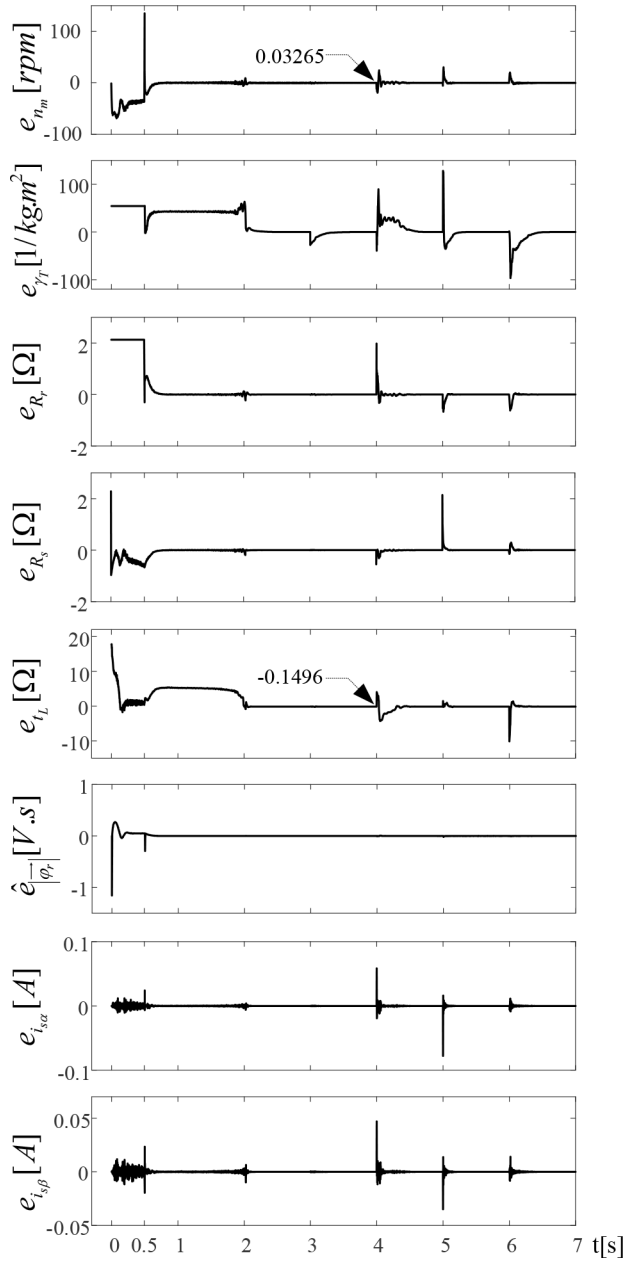
Figure 6. Simulation results for the estimation and tracking errors.

Analyzing the estimation results and the control performance in all six scenarios, the following observations are made:

- Although the initial values of all estimated states and parameters are taken as zero, the estimations beginning at $0\,s$ and $0.5\,s$ shown in Figures 5 and 6, converge to and track the actual ones.

- During $0\,s \leq t \leq 0.5\,s$, the estimations are stable but include errors, as can be seen in Figure 6, since BI-EKF performs the simultaneous estimations by using only Model-$R_s \& t_L$ with the incorrect $R_r = 0.5 \times R_{rn}$ and $\gamma_T = 0.5 \times \gamma_{Tn}$ values, meaning that there is not enough information about both R_r and γ_T in Model-$R_s \& t_L$. However, these errors quickly go to zero after the BI-EKF algorithm starts the consecutive
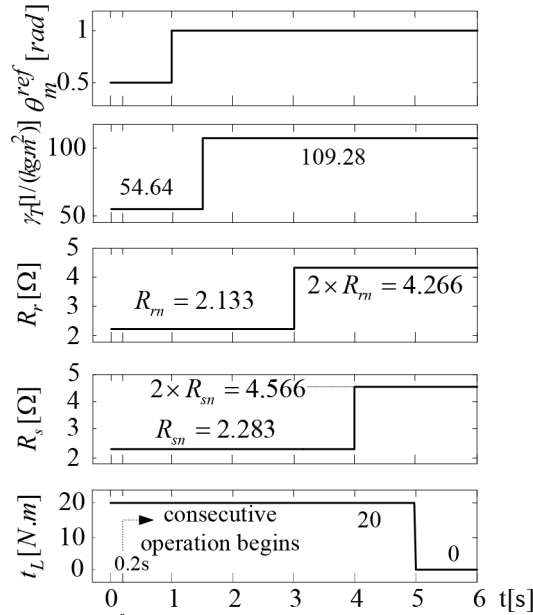
Figure 7. Variations of θ_m^{ref}, the applied t_L, R_s, R_r, and γ_T for performance test.

operation based on Model-$R_s \& t_L$ and Model-$R_r \& \gamma_T$ at every sampling time, which occurs at $0.5\,s$.

- In the time interval of $0.5\,s \le t \le 3\,s$, $\hat{\gamma}_T$ needs some time to reach the actual γ_T value ($\gamma_T = 1/j_T = 1/0.0183 = 54.64$ $(1/(kg \cdot m^2)))$, since $\hat{R}_s$ and $\hat{t}_L$ include the errors that occur due to the incorrect R_r and γ_T values used in the estimation algorithm in the previous time interval of $0\,s \le t \le 0.5\,s$. It is also observed that $\hat{\gamma}_T$ has a longer transient when ω_m is linearly changed, as in this time period of $0.5\,s \le t \le 3\,s$. In other words, the longer the linear variation in ω_m, the longer the transient in $\hat{\gamma}_T$, because $\hat{t}_L$ is defined as constant in Model-$R_s \& t_L$, even though it includes the simultaneous estimation of $t_L + \beta_T \omega_m$. However, $\hat{t}_L$ and, hence, $\hat{\gamma}_T$ quickly converge to their real values as ω_m approaches its steady-state value.

- The proposed BI-EKF algorithm is able to estimate the viscous friction term within $\hat{t}_L$. This fact can be easily revealed by the calculations below for the time interval $3\,s \le t \le 4\,s$ in Figures 5 and 6:

$$\omega_m\left(\infty\right) = \hat{\omega}_m\left(\infty\right) + e_{\omega_m(\infty)} = 2\pi\left(\frac{1430 - 0.03265}{60}\right) = 149.75$$

$$e_{t_L}\left(= t_L - \hat{t}_L\right) = -\beta_T \omega_m\left(\infty\right)$$
$$-0.1496 = -0.001 \times 149.75$$
$$-0.1496 \cong -0.1497$$

5.2. Simulation results and observations for the speed-sensorless position control system

In this section, two different groups of simulations are carried out. The first confirms the performance of the novel BI-EKF algorithm via the speed-sensorless position control system under no load and rated load at constant position (zero speed) as well as variations in R_r, R_s, and j_T as shown in Figure 7 and Figures 8(a)–8(r), which

show variations of $\theta_m^{ref}\&\hat{\theta}_m$, $\left|\hat{\vec{\varphi}}_r\right|\&|\vec{\varphi}_r|^{ref}$, $t_L\&\hat{t}_L$, $R_r\&\hat{R}_r$, $R_s\&\hat{R}_s$, $\gamma_T\&\hat{\gamma}_T$, $\varphi_{r\alpha}\&\hat{\varphi}_{r\alpha}$, $\varphi_{r\beta}\&\hat{\varphi}_{r\beta}$, $i_{s\alpha}\&\hat{i}_{s\alpha}$,

$e_{n_m} = n_m - \hat{n}_m$, $e_{|\vec{\varphi}_r|} = |\vec{\varphi}_r|^{ref} - \left|\hat{\vec{\varphi}}_r\right|$, $e_{t_L} = t_L - \hat{t}_L$, $e_{R_r} = R_r - \hat{R}_r$, $e_{R_s} = R_s - \hat{R}_s$, $e_{\gamma_T} = \gamma_T - \hat{\gamma}_T$,

$e_{\varphi_{r\alpha}} = \varphi_{r\alpha} - \hat{\varphi}_{r\alpha}$, $e_{\varphi_{r\beta}} = \varphi_{r\beta} - \hat{\varphi}_{r\beta}$, and $e_{i_{s\alpha}} = i_{s\alpha} - \hat{i}_{s\alpha}$, respectively. For this purpose, as seen in Figure 7:

- Firstly, the novel BI-EKF algorithm is given a start with incorrect $R_r = 1.3 \times R_{rn}$ and $\gamma_T = 0.5 \times \gamma_{Tn}$ under t_{Ln}, R_{sn}, and j_{Tn}, using only Model-$R_s\&t_L$ $(0\,s \leq t \leq 0.2\,s)$.

- Then the successive operation of the novel BI-EKF algorithm begins at $0.2\,s$, and the IM is kept running under rated parameters and t_{Ln} $(0.2\,s \leq t \leq 1.5\,s)$.

- Next, j_T is stepped down to $0.5 \times j_{Tn}$ at $1.5\,s$. In other words, γ_T is stepped up to $2 \times \gamma_{Tn}$ while the IM is running with t_{Ln}, R_{sn}, and R_{rn} $(1.5\,s \leq t \leq 3\,s)$.

- Following the previous scenario, R_r and R_s are instantly increased to $2 \times R_{rn}$ at $3\,s$ and $2 \times R_{sn}$ at $4\,s$, respectively $(3\,s \leq t \leq 5\,s)$.

- Finally, the IM is instantly unloaded when it is operating with $2 \times R_{sn}$, $2 \times R_{rn}$, and $2 \times \gamma_{Tn}$ $(5\,s \leq t \leq 6\,s)$.

Considering the challenging scenarios above:

- It is observed that the proposed BI-EKF algorithm is able to handle the incorrect R_r and γ_T values in the time intervals of $0\,s \leq t \leq 0.2\,s$, because errors in all estimated states and parameters immediately go to zero during $0\,s \leq t \leq 0.2\,s$, as seen in Figures 8(a)–8(r).

- $\hat{i}_{s\alpha}$, $\hat{i}_{s\beta}$, $\hat{\varphi}_{r\alpha}$, $\hat{\varphi}_{r\beta}$, $\hat{\omega}_m$, $\hat{t}_L$, $\hat{R}_s$, $\hat{R}_r$, and $\hat{\gamma}_T$ converge real ones. Thus, θ_m^{ref} and $|\varphi_r|^{ref}$ are well-controlled by the speed-sensorless position control system.

- All the results obtained in this study are unique, according to the literature, because they are obtained at constant position (zero speed). Especially during the time range of $5\,s \leq t \leq 6\,s$, the dc condition takes place, which is the worst case [16] for IM parameter and state estimations. However, the proposed algorithm is able to estimate nine states and parameters in total without the utilization of the high frequency signal injection methods stated in [16].

The second group of simulations is performed in order to show the superiority of the proposed BI-EKF algorithm over the past study [17], which estimates all state and parameters as in this study, except for γ_T (or $1/\gamma_T$). To achieve this aim, the scenarios shown in Figure 9 are used, and the resulting estimation performances are depicted in Figures 10(a)–10(o). Figure 10 illustrates the variations of $\theta_m^{ref}\&\hat{\theta}_m$ in Figures 10(a) and 10(b), $\left|\hat{\vec{\varphi}}_r\right|\&|\vec{\varphi}_r|^{ref}$ in Figures 10(c) and 10(d), $t_L\&\hat{t}_L$ in Figures 10(e) and 10(f), $R_r\&\hat{R}_r$ in Figures 10(g) and 10(h), $R_s\&\hat{R}_s$ in Figures 10(i) and 10(j), $\hat{\varphi}_{r\alpha}\&\hat{\varphi}_{r\beta}$ in Figures 10(k) and 10(l), $e_{\theta_m} = \theta_m^{ref} - \hat{\theta}_m$ in Figures 10(m) and 10(n), and $\gamma_T\&\hat{\gamma}_T$ in Figure 10(o). In this scenario, the proposed BI-EKF and the braided EKF in [17] start the consecutive operation at $0.2\,s$ and $0.5\,s$, respectively, and j_T is stepped down to $0.5 \times \gamma_{Tn}$ (or γ_T is stepped up to $2 \times \gamma_{Tn}$) at $1.5\,s$ under t_{Ln}, R_{sn}, and R_{rn} for a constant position of the IM. Under this variation, the estimation performance of the braided EKF algorithm in [17] gets worse, as seen in Figures 10(a)–10(o), since the braided EKF algorithm does not take j_T (γ_T)-estimation into account. On the other hand, the novel

BI-EKF algorithm shows very acceptable estimation performance under j_T variation. These results request j_T-estimation together with the estimations of $i_{s\alpha}$, $i_{s\beta}$, $\varphi_{r\alpha}$, $\varphi_{r\beta}$, ω_m, R_r, and t_L for such a motion control application, which involves the inertia variation. Note that the novel BI-EKF algorithm has the spikes on the estimated states at the instant the consecutive operation begins, due to switching two unknown states ($R_r\&j_T$)
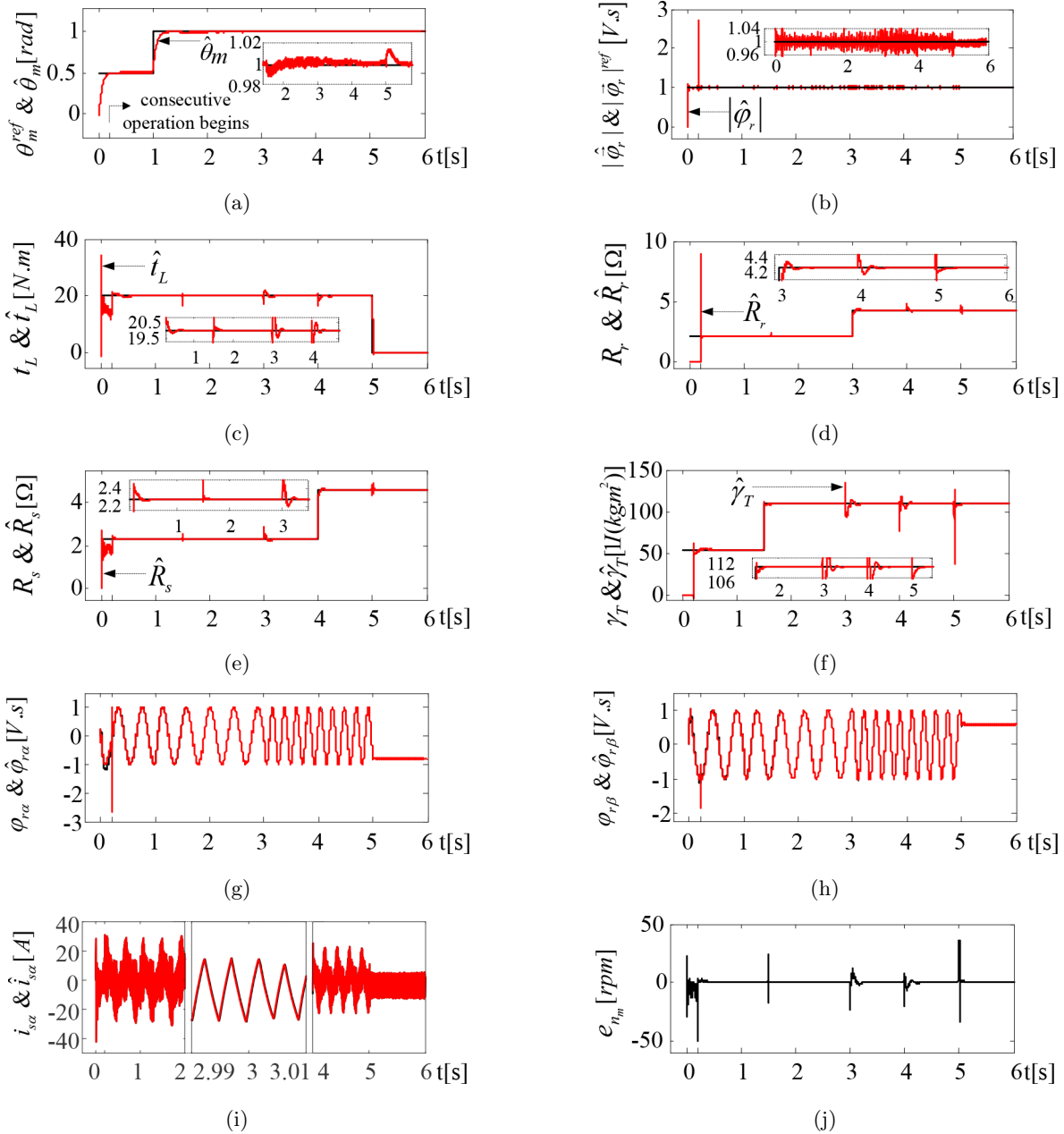

Figure 8. Simulation results of novel BI-EKF based estimator and the speed-sensorless position control system: (a) variations of $\theta_m^{ref}\&\hat{\theta}_m$; (b) variations of $\left|\hat{\vec{\varphi}}_r\right|\&|\vec{\varphi}_r|^{ref}$; (c) variations of $t_L\&\hat{t}_L$; (d) variations of $R_r\&\hat{R}_r$; (e) variations of $R_s\&\hat{R}_s$; (f) variations of $\gamma_T\&\hat{\gamma}_T$; (g) variations of $\varphi_{r\alpha}\&\hat{\varphi}_{r\alpha}$; (h) variations of $\varphi_{r\beta}\&\hat{\varphi}_{r\beta}$; (i) variations of $i_{s\alpha}\&\hat{i}_{s\alpha}$; (j) variations of $e_{n_m} = n_m - \hat{n}_m$.
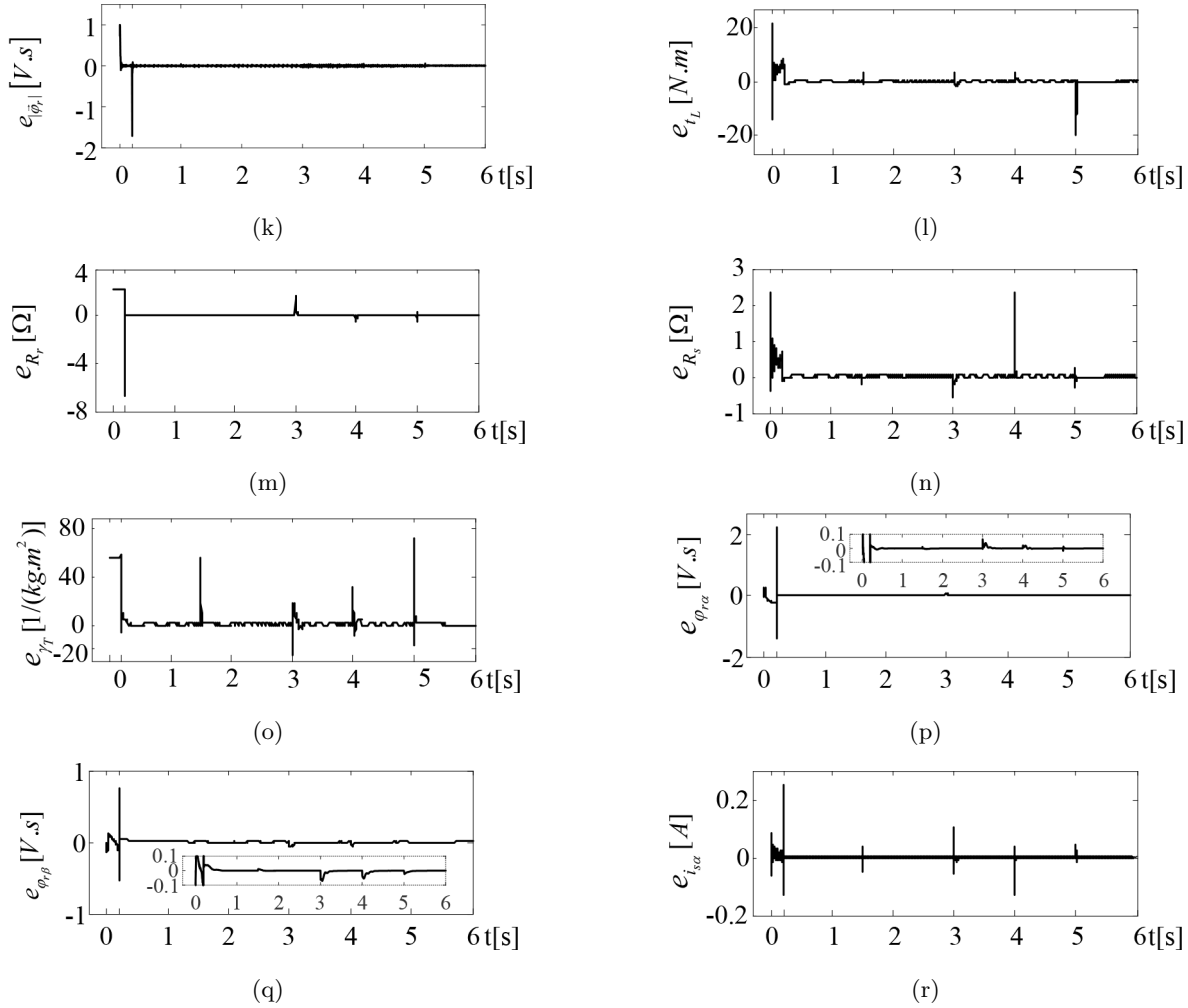
Figure 8. Simulation results of novel BI-EKF based estimator and the speed-sensorless position control system: (k) variations of $e_{|\vec{\varphi}_r|} = |\vec{\varphi}_r|^{ref} - \left|\hat{\vec{\varphi}}_r\right|$; (l) variations of $e_{t_L} = t_L - \hat{t}_L$; (m) variations of $e_{R_r} = R_r - \hat{R}_r$; (n) variations of $e_{R_s} = R_s - \hat{R}_s$; (o) variations of $e_{\gamma_T} = \gamma_T - \hat{\gamma}_T$; (p) variations of $e_{\varphi_{r\alpha}} = \varphi_{r\alpha} - \hat{\varphi}_{r\alpha}$; (q) variations of $e_{\varphi_{r\beta}} = \varphi_{r\beta} - \hat{\varphi}_{r\beta}$; and (r) variations of $e_{i_{s\alpha}} = i_{s\alpha} - \hat{i}_{s\alpha}$.

in the BI-EKF algorithm differently from the braided EKF algorithm, where a single unknown state (R_r) is switched.

6. Experimental results

In order to validate the novel BI-EKF algorithm in real time, the experimental setup shown in Figure 11 is utilized as in [12]. The setup consists of:

- a squirrel cage type IM with the following specifications: 3-phase, 6-pole, 380 V, 5.9 A, 2.2 kW, 22 $N.m$, 940 rpm, $R_s = 3.03$ Ω, $R_r = 2.88$ Ω, $L_{ls} = 0.0124$ H, $L_{ls} = 0.0186$ H, and $L_m = 0.1843$ H, $\gamma_T = 1/j_T = 0.056 = 17.85$ $(kg \cdot m^2)^{-1}$;
- a Foucault brake with 30 $N.m$ driven for loading the IM by hand with the utilization of a step-like variable dc source;
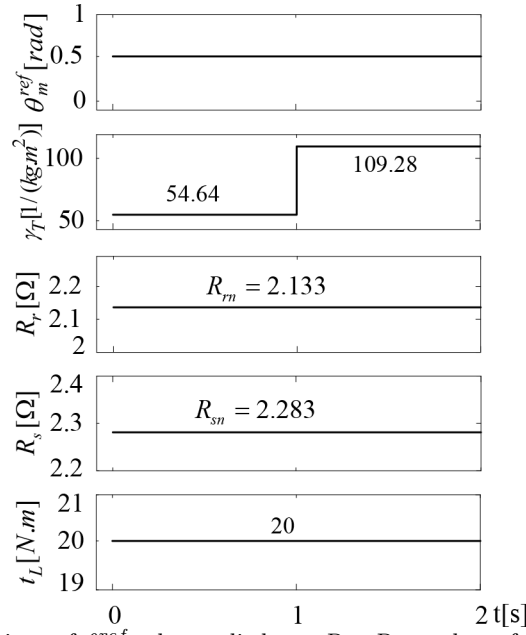
Figure 9. Variations of θ_m^{ref}, the applied t_L, R_s, R_r, and γ_T for comparison test.
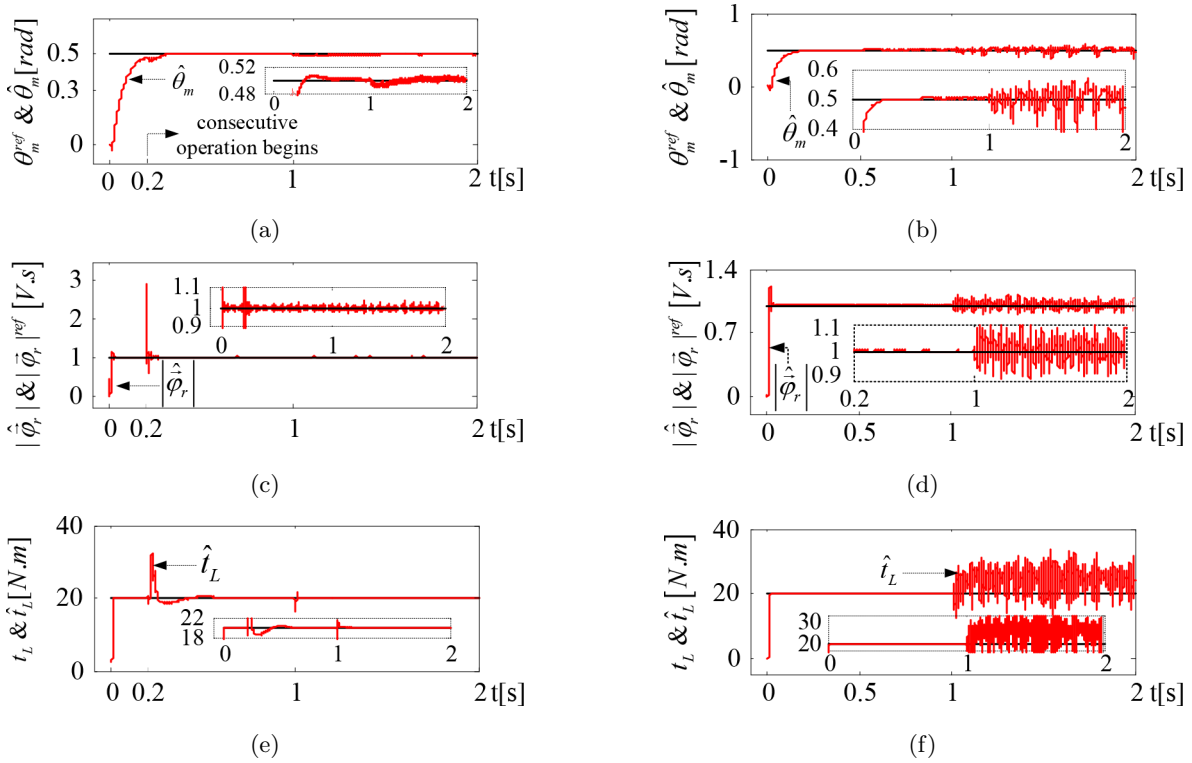

(a)

(b)

(c)

(d)

(e)

(f)

Figure 10. Comparative results for variations in j_T: (a) and (b): variations of $\theta_m^{ref} \& \hat{\theta}_m$; (c) and (d): variations of $\left|\hat{\vec{\varphi}}_r\right| \& |\vec{\varphi}_r|^{ref}$; (e) and (f): variations of $t_L \& \hat{t}_L$.
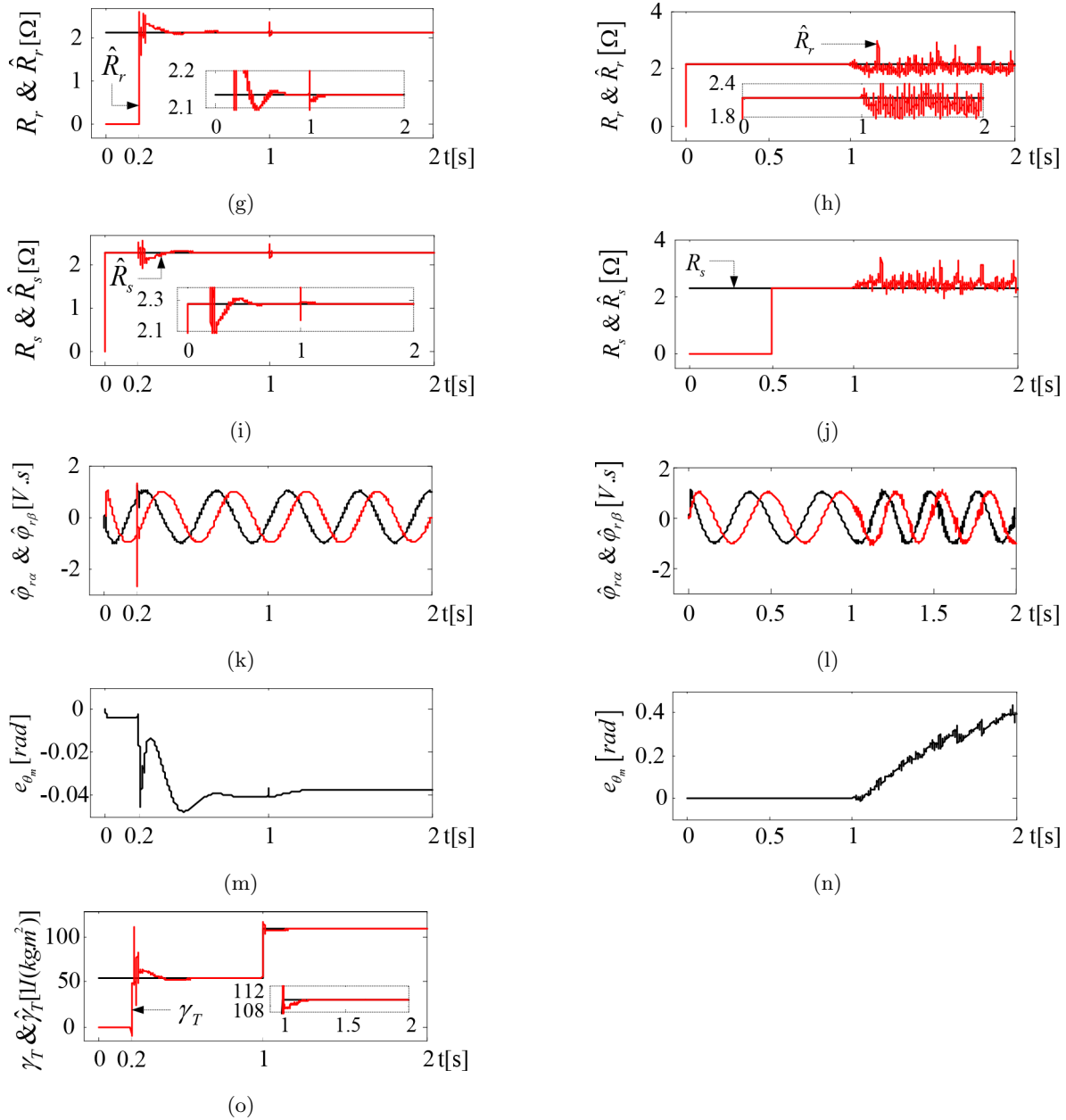
(g)

(h)

(i)

(j)

(k)

(l)

(m)

(n)

(o)

Figure 10. Comparative results for variations in j_T: (g) and (h): variations of $R_r \& \hat{R}_r$; (i) and (j): variations of $R_s \& \hat{R}_s$; (k) and (l): variations of $\hat{\varphi}_{r\alpha} \& \hat{\varphi}_{r\beta}$; (m) and (n): variations of $e_{\theta_m} = \theta_m^{ref} - \hat{\theta}_m$; (o): variations of $\gamma_T \& \hat{\gamma}_T$.

- a PC-based DS1104 controller board, processing floating-point operations at a rate of 250 MHz for implementing the BI-EKF algorithm;
- an encoder with 5000 lines/rev and a torque transducer with 50 $N.m$, which are only utilized for confirming ω_m (n_m r/min) and t_L estimations, respectively;
- LV100-400 and LA55-P/SP1 for measuring the phase voltages and currents, respectively;
- a manually adjustable three-phase array resistor connected in series to the stator windings of the IM for generating variations in R_s and validating R_s-estimation.
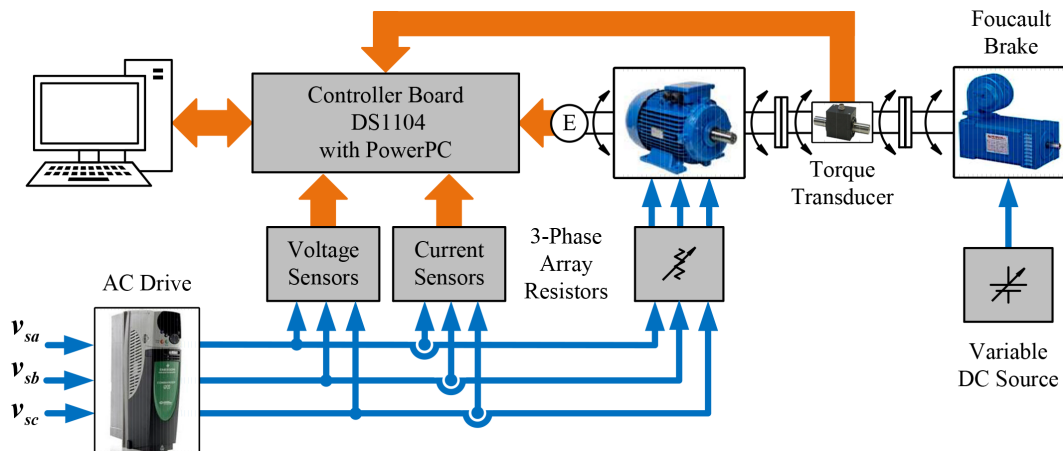
Figure 11. Experimental setup utilized for validating the novel BI-EKF algorithm.

6.1. Optimizing covariance matrices of the novel BI-EKF algorithm via genetic algorithm

As the number of estimated states and parameters in real-time are increased by EKF algorithms, determining the elements of Q_i and D_ξ with a trial-and-error process becomes more difficult and may not give the best estimation performance. Thus, the method in [23], which minimizes the fitness function defined as the mean squared error between the real and estimated rotor angular velocities via a real coded genetic algorithm (GA) for obtaining the elements of Q and D_ξ, is used for Q_i and D_ξ in this study, with the assumption of $P_i = diag\left\{\ 9\quad 9\quad 9\quad 9\quad 9\quad 9\quad 9\ \right\}$. The optimal performance of the novel BI-EKF algorithm is obtained with:

$$Q_1 = diag\left\{\begin{array}{cccc} 7.3130 \times 10^{-4} & 7.3130 \times 10^{-4} & 1.2512 \times 10^{-6} & 1.2512 \times 10^{-6} \\ 9.7980 \times 10^{-5} & 3.2150 \times 10^{-4} & 4.4677 \times 10^{-6} \end{array}\right\}$$

$$Q_2 = diag\left\{\begin{array}{cccc} 4.9933 \times 10^{-9} & 4.9933 \times 10^{-9} & 4.0625 \times 10^{-9} & 4.0625 \times 10^{-9} \\ 4.3568 \times 10^{-10} & 2.2058 \times 10^{-9} & 5.9206 \times 10^{-7} \end{array}\right\}$$

$$D_\xi = diag\left\{\ 1\quad 1\ \right\}$$

6.2. Real-time experimental results

With the help of the experimental setup shown in Figure 11 and previously used in [12], the proposed BI-EKF algorithm-based states and parameter estimations are verified in real time, and the obtained results are presented in Figure 12. Here t_{ind} represents the induced torque obtained from the torque transducer, and "^" refers to estimated state or parameter. Figure 12 consists of the following scenarios:

(i) Start-up: The IM and the proposed BI-EKF algorithm are given a start. The start speeds up from $0\,rpm$ to $952\,rpm$ in $1\,s$, and is loaded from $0\,N.m$ to $17.5\,N.m$. During $0 \leq t \leq 9.7\,s$, due to the externally connected serial three-phase array resistor to the stator windings of $1.5\,\Omega$, R_s is equal to $R_{sn} + 1.5\,\Omega$, and the consecutive operation begins at $2.07\,s$.

(ii) Velocity and load torque reversals: Since the input frequency of the ac drive is linearly changed from $50\,Hz$ to $-50\,Hz$ and vice versa at $9.7\,s$ and $31.9\,s$, respectively, the rotor angular velocity and thus the load torque are reversed.
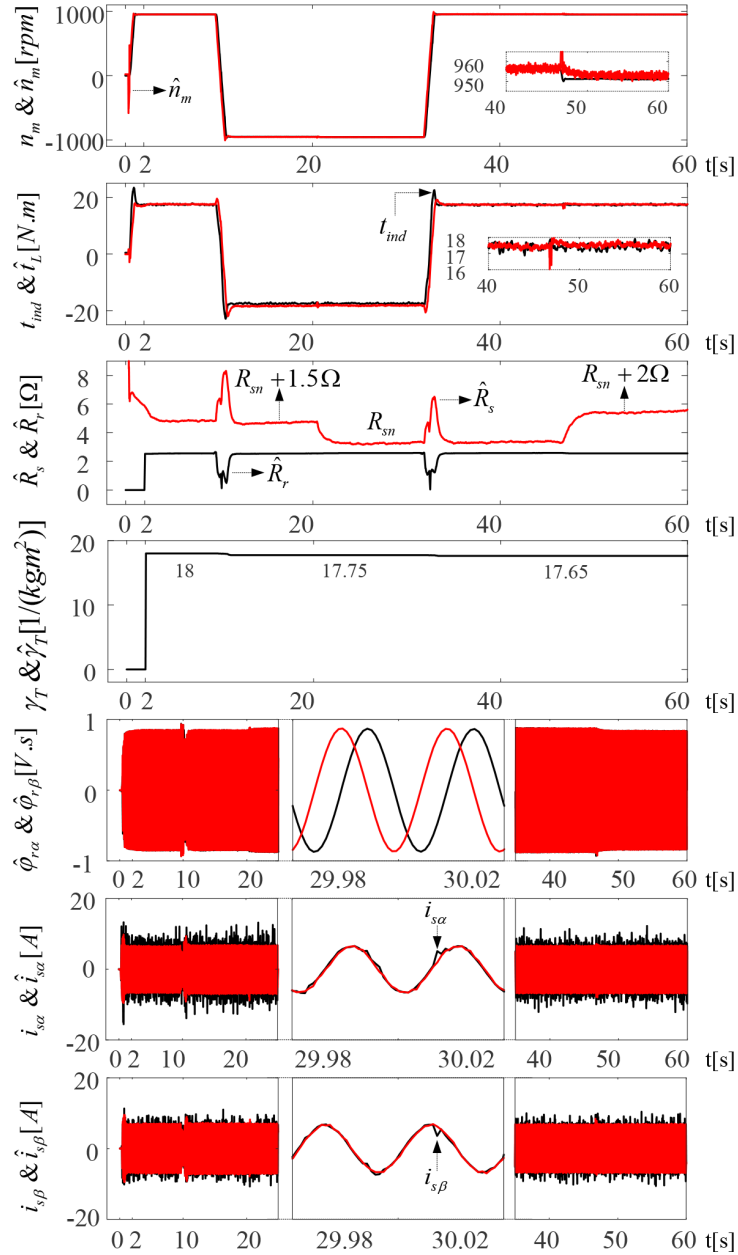
Figure 12. Real-time experimental results of the novel BI-EKF algorithm.

(iii) Variations in R_s: R_s is stepped down to R_{sn} at $20.4\,s$ by disconnecting the external three-phase array resistor, and then R_s is instantly increased to $R_{sn} + 2\,\Omega$ at $46.6\,s$.

Inspecting the results obtained under the challenging scenarios above, it is observed that:

- all of the estimated states and parameters converge with real ones with very good precision;

- the proposed BI-EKF algorithm is able to perform estimations in a wide speed range, including zero crossovers;

- the estimations demonstrated in this study are in harmony with those presented in [18]. However, differently from [18], this study also presents $\hat{\gamma}_T$.

In summation, the achieved results validate that the novel BI-EKF algorithm proposed in this study is implementable in real-time and has satisfactory estimation performance.

7. Conclusion

In this study, a novel BI-EKF-based estimation technique is firstly introduced into the literature in order to increase the number of estimated states and parameters presented in its previous version [18]. It is tested with real time-experiments, in addition to a rotor flux oriented speed-sensorless DVC system developed for either velocity or position control of IMs in simulations. In spite of its computational complexity, the novel BI-EKF algorithm simultaneously estimates the stator stationary axis components of stator currents and rotor fluxes, rotor angular velocity, load torque including the viscous friction term, stator and rotor resistance, and the reciprocal of total inertia with the utilization of the measured stator phase voltages and currents. Thus, it improves the performance of the speed-sensorless velocity and position control systems in both transient and steady states. The simulations, including the challenging variations of stator and rotor resistances, load torque, total inertia, and velocity/position reference, prove that the proposed speed-sensorless DVC systems have superiority over the previous EKF schemes, as in [17,18]. The real-time experiments also confirm that the proposed BI-EKF algorithm is realizable and able to estimate all the states and parameters with very good accuracy. Moreover, differently from the study in [20], which estimates all the varying electrical parameters (stator and rotor resistances and magnetizing inductance) as well as the estimations of stator currents and rotor fluxes, rotor angular velocity, and load torque, including viscous friction term especially for working in the field-weakening region, this study has focused on estimating all the varying mechanical parameters (load torque with inclusion of viscous friction term and the reciprocal of total inertia), as well as the estimations of stator currents and rotor fluxes, rotor angular velocity, and stator and rotor resistances for very low speed operations that require correct inertia information.

Acknowledgment

References

[1] Schauder C. Adaptive speed identification for vector control of induction motors without rotational transducers. IEEE T Ind Appl 1992; 28: 1054-1061.

[2] Barut M, Bogosyan S, Gokasan M. Speed-sensorless estimation for induction motors using extended Kalman filters. IEEE T Ind Electron 2007; 54: 272-280.

[3] Gadoue SM, Giaouris D, Finch JW. Stator current model reference adaptive systems speed estimator for regenerating-mode low-speed operation of sensorless induction motor drives. IET Electr Power Appl 2013; 7: 597-606.

[4] Orlowska-Kowalska T, Dybkowski M. Stator-current-based MRAS estimator for a wide range speed-sensorless induction-motor drive. IEEE T Ind Electron 2010; 57: 1296-1308.

[5] Hajian M, Soltani J, Markadeh GA, Hosseinnia S. Adaptive nonlinear direct torque control of sensorless IM drives with efficiency optimization. IEEE T Ind Electron 2010; 57: 975-985.

[6] Aydeniz MG, Şenol I. A Luenberger-sliding mode observer with rotor time constant parameter estimation in induction motor drives. Turk J Electr Eng & Comp Sci 2011; 19: 901-912.

[7] Vicente I, Endemano A, Garin X, Brown M. Comparative study of stabilising methods for adaptive speed sensorless full-order observers with stator resistance estimation. IET Control Theory Appl 2010; 4: 993-1004.

[8] Verma V, Chakraborty C, Maiti S, Hori Y. Speed sensorless vector controlled induction motor drive using single current sensor. IEEE T Energy Conver 2013; 28: 938-950.

[9] Chang C, Liu C. A new MRAS-based strategy for simultaneous estimation and control of a sensorless induction motor drive. J Chin Inst Eng 2010; 33: 451-462.

[10] Zhao L, Huang J, Liu H, Li B, Kong W. Second-order sliding-mode observer with online parameter identification for sensorless induction motor drives. IEEE T Ind Electron 2014; 61: 5280-5289.

[11] Tajima H, Guidi G, Umida H. Consideration about problems and solutions of speed estimation method and parameter tuning for speed-sensorless vector control of induction motor drives. IEEE T Ind Appl 2002; 38: 1282-1289.

[12] Ha IJ, Lee SH. An online identification method for both stator and rotor resistances of induction motors without rotational transducers. IEEE T Ind Electron 2000; 47: 842-853.

[13] Zhen L, Xu L. Sensorless field orientation control of induction machines based on a mutual MRAS scheme. IEEE T Ind Electron 1998; 45: 824-831.

[14] Barut M, Bogosyan S, Gokasan M. Switching EKF technique for rotor and stator resistance estimation in speed sensorless control of IMs. Energy Convers Manag 2007; 48: 3120-3134.

[15] Barut M, Bogosyan S, Gokasan M. Experimental evaluation of braided EKF for sensorless control of induction motors. IEEE T Ind Electron 2008; 55: 620-632.

[16] Bogosyan S, Barut M, Gokasan M. Braided extended Kalman filters for sensorless estimation in induction motors at high-low/zero speed. IET Control Theory A 2007; 1: 987-998.

[17] Barut M, Bogosyan S. Sensorless sliding mode position control of induction motors using braided extended Kalman filters. In: IEEE 2007 International Symposium on Industrial Electronics; 4–7 June 2007; Vigo, Spain. New York, NY, USA: IEEE. pp. 2268-2273.

[18] Barut M, Demir R, Zerdali E, Inan R. Real-time implementation of bi input-extended Kalman filter-based estimator for speed-sensorless control of induction motors. IEEE T Ind Electron 2012; 59: 4197-4206.

[19] Barut M. Bi-input extended Kalman filter based speed-sensorless vector control of induction motors with the estimations of rotor and stator resistances, load torque, and inertia. In: IEEE 2011 International Conference on Modeling and Simulation of Electric Machines, Converters and Systems; 6–8 June 2011; Cergy-Pontoise, France. New York, NY, USA: IEEE.

[20] Inan R, Barut M. Bi input-extended Kalman filter-based speed-sensorless control of an induction machine capable of working in the field-weakening region. Turk J Electr Eng & Comp Sci 2014; 22: 588-604.

[21] Hung JY, Gao W, Hung JC. Variable structure control: a survey. IEEE T Ind Electron 1993; 40: 2-22.

[22] Sahin C, Sabanovic A, Gokasan M. Robust position control based on chattering free sliding modes for induction motors. In: IEEE 1995 International Conference on Industrial Electronics, Control, and Instrumentation; 6–10 November 1995; Orlando, FL, USA. New York, NY, USA: IEEE. pp. 512-517.

[23] Shi KL, Chan TF, Wong YK, Ho SL. Speed estimation of an induction motor drive using an optimized extended Kalman filter. IEEE T Ind Electron 2002; 49: 124-133.